PCCP

Accepted Manuscript

ROYAL SOCIETY OF CHEMISTRY

www.rsc.org/pccp

PCCP

ARTICLE

Cite this: DOI: 10.1039/x0xx00000x

Received 00th January 2015,
Accepted 00th January 2015

DOI: 10.1039/x0xx00000x

www.rsc.org/

Tip-Enhanced Raman Spectroscopy of Graphene-like and Graphitic Platelets on Ultraflat Gold Nanoplates

Farshid Pashaee,[a] Faranak Sharifi,[b] Giovanni Fanchini[b] and François Lagugné-Labarthet*,[a]

In this study, tip-enhanced Raman spectroscopy (TERS) is used to characterize graphene-like and graphitic platelets composed of a few layers of graphene. Specifically, gap-mode TERS geometry provides a larger enhancement of the local electromagnetic field at the junction formed by a gold sharp tip and a gold substrate. Graphene-like platelets are deposited onto ultra-flat thin gold nanoplates using a surfactant-assisted method. Au-coated atomic force microscopy (AFM) tips are used to probe specific substrate regions coated by the platelets. TERS spectra are collected on distinctive points on the graphene-like layers and surrounding substrate using radially or linearly polarized light, with an excitation wavelength of 632.8 nm. The position, width and intensity of G, D, and 2D Raman-active modes of graphene are discussed as a function of the incident light polarization and for distinct positions on the graphene layer. We report here on the nature of the collected TERS spectra focusing in particular on the edges of the graphene platelets.

Introduction

Carbon-based materials play a major role in today's science and technology. In particular, graphene is well known for its unique electrical and mechanical (robustness, flexibility) properties. The scalability of graphene devices to nanoscale dimensions[1, 2] makes them promising candidates for applications in nano-optoelectronics. Ideally, characterization tools suitable for investigating graphene-based materials should be fast and non-destructive. They must offer high spatial and spectral resolution, provide structural and electronic information, and should be applicable at both laboratory and mass production scales.

In the last two decades, Raman spectroscopy has emerged as a powerful and non-destructive technique to characterize the electronic properties and vibrational modes of a wide range of carbon nanostructures, including graphene. The micro-Raman spectrum of few-layer graphene has been studied in great detail by Ferrari et al.[3-5] as a function of the number of layers as well as the characteristics of the graphene edges. Raman spectra are relatively similar in graphene and graphite, but some differences exist due to the missing interactions between stacked layers in graphene. Raman spectroscopy is one of the most widely used methods to investigate carbon materials.[6-10] However, at the scale of a single graphene flake, micro-Raman spectroscopy is limited in terms of spatial resolution by the Abbe's criterion.[11, 12] Although not yet a turn-key instrument, tip-enhanced Raman spectroscopy has matured over the past decade as a characterization probe with sub-wavelength imaging capabilities and is becoming a suitable tool for leading to spatial resolutions in the 10-50 nm range in optimal conditions.[13-18]

TERS is a unique characterization technique combining the capabilities of Raman spectroscopy to reveal the chemical composition of solids with the high spatial resolution of scanning probe microscopy (SPM). It can be used to obtain spectroscopic analysis of a large variety of, surfaces, materials and biomaterials with a resolution merely depending on the probe geometry.[13, 19-26] Recent publications report TERS measurements with single molecule sensitivity when performed under ultrahigh vacuum conditions. [27-29]

In TERS experiments, signal enhancement is generated by the excitation of surface plasmons localized at a metallic SPM tip apex by means of its coupling with the Raman modes of the specimen. Interaction between the tip apex and the near-field component of Raman-scattered radiation is achieved by approaching the tip to within a few nanometers of the sample's surface, which creates an increase in the observed Raman signal originating from a region determined by the radius of the tip's apex that is scanning the surface.[30, 31] Tip apices used for TERS are typically in the 10-30 nm diameter range for commercial SPM probes coated with a thin metallic layer such as gold or silver and the excitation light must have a polarization component along the tip axis.[32, 33] The use of ultraflat gold nanoplates used in conjunction with the TERS tip was pioneered by Deckert et al. to enhance further the intensity of the near-field signal of the local Raman measurements and was later applied to the study of self-assembly monolayers.[34-37] In addition of improved surface sensitivity due to local electromagnetic field enhancement in the vicinity of the tip, the significant increase in spatial resolution allows to explore a variety of surface-related questions of materials and biomaterials at the nanoscale level.[38-40]

In this report, we present TERS analysis of graphene-like and graphitic platelets composed of 7-12 layers of graphene. These layers are deposited onto thin and smooth gold nanoplates to serve as metallic substrates to perform TERS gap-mode measurements. TERS measurements have already been reported by several groups,[41, 42] and the work of Stadler et al. has focused on the detection of smaller defects on single layer graphene deposited on copper.[43] Herein, we use TERS to detect subtle structural features at the edges of the graphene-like platelets. Furthermore, we evaluate the effect of polarization of the input excitation using a tightly focused beam that is linearly and radially polarized at the selected wavelength of 632 nm.

Material and methods

Preparation of gold nanoplate substrates

Synthesis of gold (111) nanoplates was carried out using the method reported by Pashaee et al.[36] based on the initial work of Chu et al.[44] Once large gold nanotriangles were obtained, the solution was transferred to an amine-coated test tube for further purification of the gold nanoplates by centrifugation (4000 rpm for 10 min for 5-6 times). The test tubes used for centrifugation were coated with APTMS by evaporation at 130 ˚C. Trapping of the gold nanoplates on the side walls of the test tubes was effective, preventing their aggregation at the bottom of the tube centrifugation. The gold nanoplates were subsequently released by sonication followed by drop-casted onto clean glass coverslips (120 µm thickness). AFM characterization of individual nanoplates shows roughness in the range of about 500 pm.

Exfoliation and Deposition of graphene flakes on gold nanoplates.

Few-layer graphene films were deposited on glass substrates decorated with gold nanoplates using the method originally developed by Wu et al.[45] for single-wall carbon nanotubes, adapted by Eda at al.[46] for graphene oxide and further developed by Sharifi et al.[47] for surfactant-exfoliated graphene flakes. Graphite (Sigma Aldrich Inc., 332461) is used as a starting material for this process and was ultrasonicated for 24h in a 3:1 H_2SO_4:HNO_3 mixture, mildly oxidized in Piranha reagent (H_2SO_4:H_2O_2=4:1) and subsequently dried prior to further use. 6 mg of the resulting material were ultrasonicated for 4h in a 0.6 g/L water solution of RNA that acts as a non-ionic surfactant to exfoliate graphite in thin sheets of graphene.[47] The slurry produced by ultrasonication was left to sediment overnight at 2˚C in a beaker. The top three-quarters of the suspension were centrifuged at 6000 rpm for 1h, and the supernatant, largely consisting in weakly oxidized and well dispersed few- and single-layer graphene flakes,[47] was collected and used for graphene flake deposition.

The deposition process basically consists in three steps: i) 5 ml of water suspension of graphene flakes and RNA (extracted from *torulla utilis*-Aldrich) is vacuum-filtrated through a 220-nm pore size nitro-cellulose filtration membrane, which leads to the deposition of graphene flakes on the membrane if sufficiently small amounts of diluted suspensions are used to prevent re-aggregation of the flakes; ii) the filtration membrane loaded with graphene flakes is subsequently transferred onto the requisite substrate, previously decorated with gold nanoplates and is dried under load in a vacuum desiccator. iii) finally the filtration membrane is etched in consecutive acetone and methanol baths, leaving behind a random distribution of graphene domains and RNA aggregates on their substrate.

The samples were annealed on a hot plate at 540 ˚C for 30 min inside a VAC Nexus glovebox purged with nitrogen, at oxygen and moisture levels less than 2 ppm. The annealing process is known to remove the residuals of RNA from graphene.[47] Extensive characterization, including atomic force microscopy, scanning electron microscopy and conventional Raman spectroscopy was previously used to investigate the results of this process, which results in more than 50% clean graphene flakes with less than 5 layers.[47] In our case, some of these flakes are situated on top of the gold platelets and have been used for tip-enhanced Raman studies.

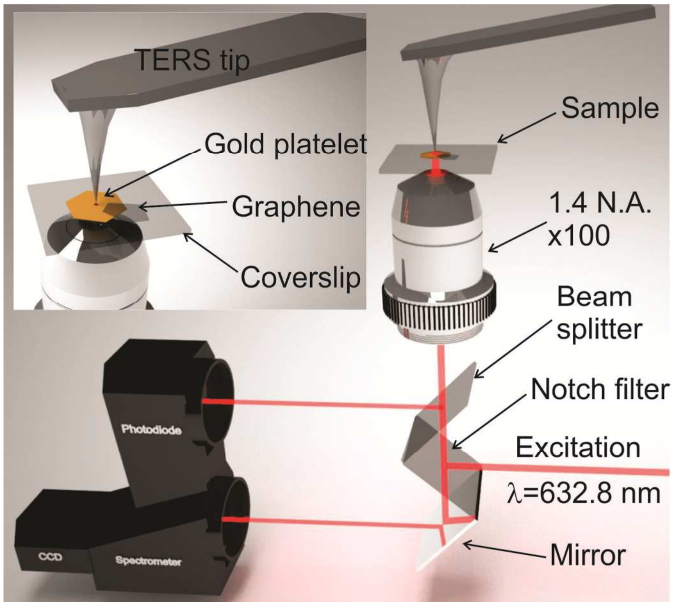

Figure 1: TERS setup in back-scattering geometry.

TERS setup

Our TERS setup combines a Raman spectrometer (HR LabRam, Horiba) attached to an inverted optical microscope (Olympus IX71) with a 5 axis AFM instrument (NanoWizard II equipped with a TAO stage, JPK Instruments Inc.). The three axis (x,y,z) piezo-actuator of the cantilever allows for the precise positioning of the tip within the centre of the focal point. Once alignment is performed, the x,y positions of the tip are frozen and only the z piezo is used to keep the feedback with the sample. The sample is moved with the x,y sample piezoelectric stage. Measurements are performed in the transmission mode as depicted in Fig. 1. An oil immersion objective with a numerical aperture of 1.4 and 100X magnification (PlanAPO Olympus) was used for focusing the excitation laser on the sample and for collection of the Raman signal in backscattering configuration. Raman-scattered photons were detected using a liquid nitrogen cooled CCD camera (Horiba, Symphony). A grating of 600 grooves/mm together with a 800 mm spectrometer focal length yielded a spectral resolution of ~1.5 cm^{-1}. The intensities of the excitation laser (He-Ne laser, λ=632.8 nm) were of 200 µW and

900 µW for the radial and linearly polarized modes, respectively. This power value takes into account the light absorption by the 20 nm-thick gold nanoplates on the top of which the graphene-like flakes are deposited. The AFM tip used for these experiments was prepared from commercially available silicon cantilever (NCL, NANO WORLD Innovative Technologies, f=190 kHz, k=48 N/m). These tips have been coated with a 3 nm of Ti as an adhesion layer followed by 20 nm of gold using electron-beam evaporation. Rayleigh scattering from the metallized tip was measured (Figs. 1 and 2) using a photodiode connected to the AFM control electronic in order to perform a crude alignment of the tip at the centre of the focal point. Finer alignment was then performed by optimizing the TERS signal of the sample by slightly moving the tip in the vicinity of the focal volume. Adjustment of the microscope objective position was also used to maximize the signal. When all conditions are reached the tip was frozen in the x,y position and the objective was remained untouched during the duration of the experiment.

TERS measurements were performed for various tip-sample distances ranging from the optical near-field to far-field. Line scan measurements were performed at nanoscale resolution using step of 5 nm between two adjacent points. All Raman spectra were recorded in the 1000–3000 cm^{-1} spectral range. Laser excitation was either linearly polarized or was modified using a liquid crystal modulator with phase compensation (ARCoptix) to obtain radially polarized light. The size of the beam was adjusted to fill the entrance pupil of the objective. Focussed radially polarized light mode includes a z-polarized component of the electric field located at the centre of the focal spot that yields the largest Raman signal enhancement when interacting with the AFM tip. Still, the intensity of the z component is small compared to the x and y polarization components as far as only Rayleigh scattering is considered. A significant z-component is only associated to the TERS signal.

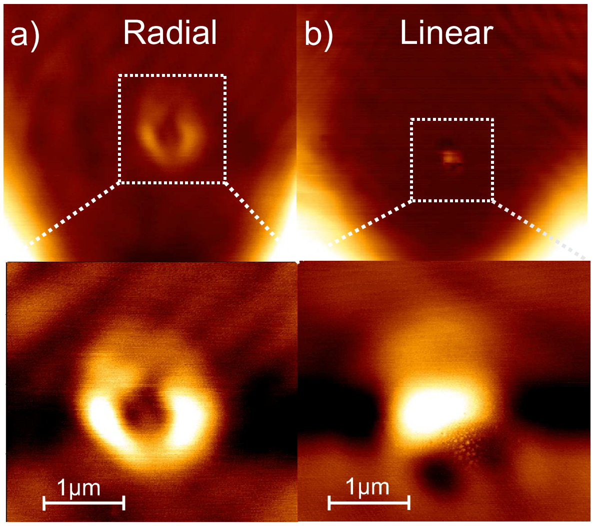

Figure 2: Scattered laser light from the tip apex under radial (a) and linearly polarized (b) polarization configurations.

Results and Discussion

In TERS, it is critical that the laser beam is tightly focused at the apex of the metallized tip. To align the laser beam coincidentally with the AFM probe, we first measured the Rayleigh scattering from the tip that scans the fixed focal volume of the excitation beam. Figs. 2a and 2b show the scattering maps measured from a radial and linearly polarized beams, respectively. Once the tip is coincidental with respect to the excitation light and brought in feedback with the surface of the sample, the sample stage is used to scan the sample along the x and y directions while the z feedback of the tip is maintained using the z piezo actuator of the tip.

In our experiments, flat gold nanoplates with thickness of around 20 nm were used as substrates onto which graphene-like flakes were deposited. Figs. 3a and 3b show an AFM image and topographical profile of a few-layer graphene flake placed over an isolated Au nanoplate. As shown in Fig. 3b, the thickness of the flake is ~5 nm which corresponds to about 12 graphene layers considering that the layers float 0.4 nm above the substrate and an interlayer spacing of 0.4 nm. Typical number of layers of the exfoliated graphene flakes analysed in these specific samples varied between 7 (3 nm thick) to 12.

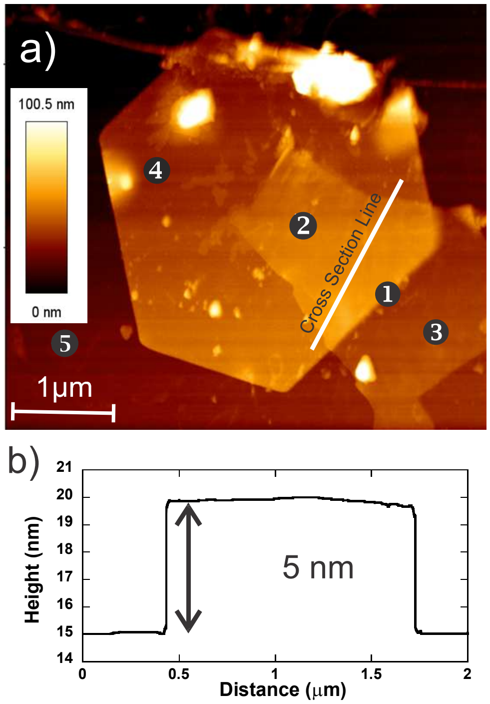

Figure 3: Atomic force microscopy (b) images of gold nanoplate partially covered with a graphene flake. (c) cross section of the few-layer graphene flake deposited onto the gold nanoplate. TERS spectra were acquired on selected points 1, 2, 3, 4, 5

TERS spectra were recorded at five different positions as indicated in Fig. 3a and are shown in Fig. 4a,b for both radially and linearly polarized excitations, respectively.

The series of spectra reported in Figs 4a,b was measured at five different locations on the graphene flake located on glass and on Au nanoplate (noted 1, 2, 3 in Fig.3a) using a 15 s acquisition time. The background signal from the gold nanoplate (point 4) and for the glass coverslip (point 5) were also collected. The strongest TERS response was recorded when the tip was positioned on the edge of gold nanoplate indicated by location in spot 1 in Fig. 3a. Enhancement at this specific edge may be a direct indicator of a large number of lattice defects induced by the bending of the graphene flake over the edge of the gold nanoplate. Additionally, increased sensitivity may occur on this feature because of the change in orientation of the graphene layer relative to the tip and resulting polarization of the enhanced field.

It is noteworthy that TERS spectra measured over the gold nanoplates in the absence of graphene (spot 4) show an intense and broad peak which is also observed on bare glass coverslips. Backscattering of the glass coverslip is most probably increased due to a mirror effect of the highly reflective metallic nanoplate+tip assembly. Possible luminescence can also be observed from the gold nanoplate interacting with the gold tip even though small laser intensities are presently used. Such effect was recently evidenced by Merlen et al. under low irradiance using 632.8 nm excitation on rough gold surfaces using near-field optical measurements with a gold tip.[48] In their work, the maximum luminescence was observed at ~1000 cm^{-1} which corresponds to the lower limit of the spectral range studied here. Luminescence was also reported on similar ultraflat gold (111) nanoplates by Viarbitskaya et al. using two photon excitation.[49] Nevertheless, in the present study, such effect is considerably reduced once the graphene layer is sandwiched between the gold plate and the metallic tip allowing one to distinguish the sharp Raman modes from graphene-like flakes from the glass background or the luminescence effect.

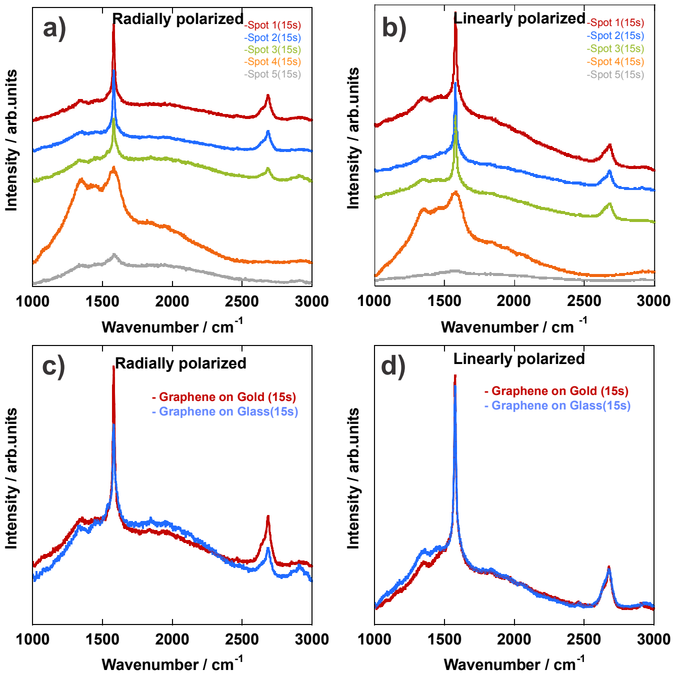

Figure 4: Tip-enhanced Raman spectra measured in 5 distinct locations shown in Fig. 3a with a radially (a) and linearly (b) polarized excitation (λ = 632 nm, acquisition time = 15 s). Selected TERS spectra of graphene deposited on gold and on glass acquired using radially (c) and linearly (d) polarized excitations..

The TERS spectra shown in Figs. 4c-d were collected using radial and linearly polarized modes for graphene flakes located on gold and on glass coverslip. Considering the transmission geometry of our setup and the thickness of the gold nanoplate (~20 nm), a significant portion of the 632.8 nm excitation is actually absorbed by the gold nanoplate and the intensity of the radial mode is 5 times lower than for the linearly polarized excitation. Even though the measured spectra have the same magnitude, the spectrum obtained using radially polarized light is actually obtained with a power of 200 μW at the sample while a power of 900 μW was used for the linearly polarized excitation.

Fig. 4c-d also highlights that the spectra show comparable magnitude when measured with linearly polarized light meanwhile the radially polarized light shows enhanced TERS contrast. We can therefore conclude that, in this specific geometry, the radial mode on gold nanoplate substrate appears more effective for TERS measurements yielding a higher enhancement of Raman signal from the graphene flake compared to using a linear polarization under the same conditions. All experiments described below were performed using a radially polarized mode.

The Raman spectrum of graphite and multilayer graphene consists of three fundamentally different sets of Raman phonon modes referenced as D, G and 2D. The fundamental defect mode appearing at 1333 cm^{-1} and is sensitive to the presence of defect in the graphene structure. Interestingly, The D peak behaves in a different way compared to the G (1580 cm^{-1}) and 2D (2684 cm^{-1}), because it is used to determine the number and orientation of layers, the quality and types of edge, and the effects of perturbations, such as electric and magnetic fields, strain, doping, disorder and functional groups.[43, 50] In graphene study, defects play a critical role and their identification, quantification and manipulation allows one to enable a wider range of promising applications. The defect induced D band occurs because of a double resonance process that requires elastic scattering from a defect and inelastic scattering by a phonon. Thus, the maximum intensity of the D mode, I(D), should be measured when the focussed laser beam crosses the edges. Edges are preferred sites to attach functional groups, and their electronic and magnetic properties are different from the bulk.[43] Practically the intensity of the D band is dependent on edge type, such as whether it takes a zigzag or armchair conformation and its Raman intensity also varies with the incident polarization. For ideal edges, the D peak is absent for zigzag configuration and large for armchair, allowing in principle, the use of Raman spectroscopy as a sensitive tool to determine the edge orientation. In reality, the D to G ratio does not always show a significant dependence on edge orientation.[51] The ratio of the D to G peak intensity I(D)/I(G) may be used to identify zigzag edges, which give very low I(D)/I(G) values near 0.05 for graphene flakes obtained by micromechanical exfoliation, in contrast to intensity ratios near 0.3 reported for armchair edges.[5] For graphene flakes with only pure zigzag or armchair edges the angles formed between the edges are 2n×30º (n = 1, 2, 3 ...). In contrast, graphene flakes with neighbouring zigzag and armchair edges will have angles of (2n-1) × 30 º (e.g., 30 º, 90 º, 150 º).[52] This angle implies, for ideal edges, that if one edge is zigzag the other must be armchair or vice-versa, but the two edges cannot have the same chirality.[53] As shown in Fig. 5a-c, Raman spectra were collected along two edges of the graphene like flakes (red and blue points). The Raman spectra (Fig. 5c) and associated I(D)/I(G) ratio for both zig-zag and armchair configurations are 0.05 and 0.13, respectively. The Raman intensities used to calculate these ratios were integrated in the [1303-1348] cm^{-1} and the [1520-1642] cm^{-1} spectral ranges for the D and G modes, respectively.

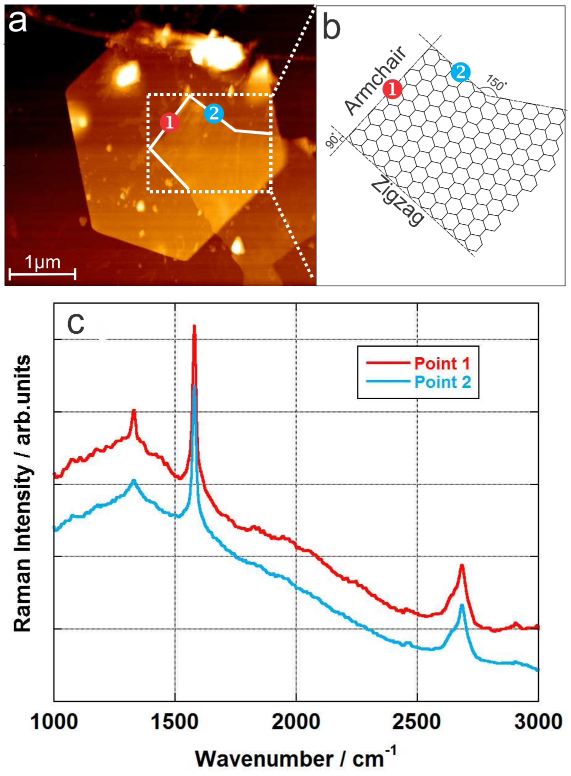

Figure 5: (a) AFM image (b) Schematic view of angles formed between two graphene edges. (c) TERS spectra measured at points 1 (red) and (2) blue.

The intensity of the D band also strongly depends on the angle between incident polarization and the graphene edge. It is maximum for polarization parallel to the edge and minimum when the polarization orientation is perpendicular to the edge.[52] Besides the relative orientation of the graphene plane with respect to the input polarization, it is also critical to evaluate the anisotropic effect due to the enhancement of the field along the direction normal to the surface (z direction). In the present case where a radial beam was used, one must consider that the TERS effect originates from the enhancement of the small component of the EM field along the z direction.[33] Such polarization-dependent enhancement has significant implication on the polarized Raman spectrum of the graphene. Depending on the angle of the resulting enhanced polarization component and its overlap with the graphene layer, the detected local intensity of specific flakes can be drastically different.

The other characteristic G peak appears around 1580 cm^{-1} and is observed in all graphitic forms and carbon structures having sp^2 hybridization (C–C bond). The intensity of the G-band should, in principle, vary linearly with the number of layers. However, it is not exactly proportional to the layer number n. Since this mode is much stronger compared to other modes, it is possible that small changes due to the variation of a small number of layers are buried under the strong intensity and are not clearly visible in the experiment.

The second order 2D band at 2684 cm^{-1} appears as a doublet and is quite sensitive to lattice perturbations affecting the vibration and electronic properties of graphene. Its position depends on the excitation wavelength but the shape of this peak gives information about the thickness of graphene.[4] Measurements where the 2D band appears as a single peak indicate the presence of a single layer graphene. When a shoulder appears at lower wavenumber of the shifted 2D main peak then it can be deduced that the graphene sheet is comprised of more than one layer. Ultimately the number of layers can be deduced by analysing the shape of the peak.[4]

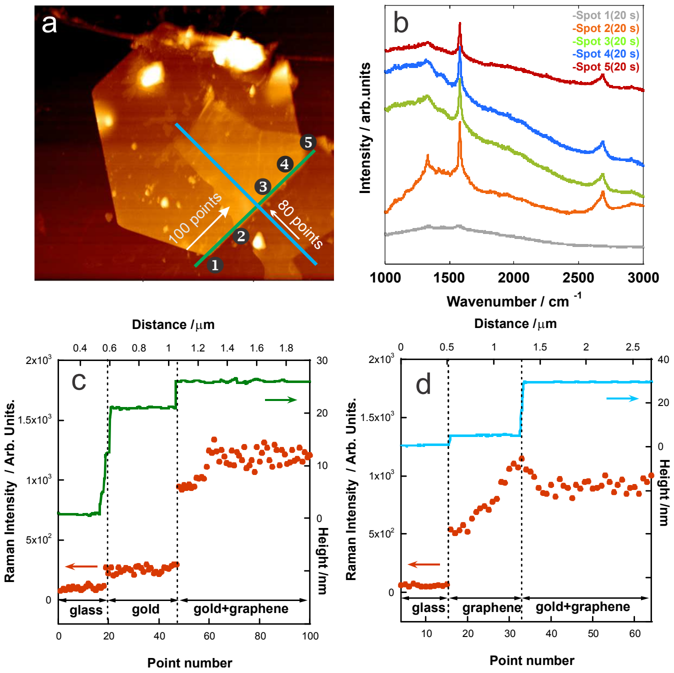

Figure 6: (a) AFM image with two cross Sections on edge boundaries and regions away from the edges. (b)TERS spectra were acquired on selected points 1,2,3,4,5 .(c) Cross Sections of sample on blue and green line. (d,e) TERS signal of G band along the scanning directions indicated in blue and green.

As depicted Fig. 6a we measured TERS signal across the edge boundaries (green line) and across an isolated graphene layers (blue line) to investigate the vibrational and electronic properties with a nanoscale spatial resolution corresponding to the tip position during the measurements at 100 points and 80 points along the arrow in two directions. The spacing between two adjacent points is ~20 nm which correspond to the typical (±5 nm) spatial resolution of our measurements.[54] Fig. 6b shows selected TERS spectra of a graphene flake located along the edge of a gold flake. When going from the outside (point 1) to the inside of the graphene sheet (point 2), the intensity of the defect peak I(D) first increases, and then decreases whereas I(G) increased moving from inside to outside the flake. First, it is noteworthy, that the shape of the 2D band shows that our graphene flakes are comprised of 5-10 layers as reported by Ferrari et al.[4] (Supplementary information SI1) confirming our estimation using AFM measurements together with interlayer spacing. Second it is important to differentiate these measurements with far-field micro-Raman results as those obtained by Casiraghi et al.[5] In their seminal study micro-Raman measurements yield a typical spatial far-field resolution of ~800 nm. This implies that the size of the diffraction limited laser spot averages a mixture of armchair and zig-zag effects thus preventing a clear cut distinction of the two types of defect at the scale of the laser spot. In our study, the significantly improved spatial resolution yields a better discrimination of the defect within the size of the localized measurement. Such improvement of spatial resolution was also pointed out by Zenobi's group showing that a spatial resolution of ~10-15 nm allowed one to identify small defects located on single-graphene layer rather than at the edges.[43] It is noteworthy that the measurements reported involve distinct samples prepared under various conductions, distinct configurations and distinct polarization and comparison must therefore be conducted with care. In Fig. 6c, we show the variation of intensity of the G mode together with the variation of the topography along the edge of the Au nanoplate. Further, point spectra were taken on the green line in Fig. 6a. Flat regions away from the edges or structural distortions typically show no enhancement of the D peak and just enhancement in the G peak and 2D peak (Spots 3, 4, 5). Fig. 6d shows a significant increase of the G mode at the edge formed by the assembly of graphene and gold platelet. The signal decrease once on the flat portion of the assembly.

The spectra shown in Fig. 7a shows the influence of the gold tip proximity from the graphene layer varying from near-field (tip in feedback) to far-field (tip 90 and 1000 nm away from the surface). Most of the Raman intensity is lost when the tip is located 1 micron above the sample confirming the near-field nature of the enhanced near-field signal. A complete series of Raman spectra was acquired by changing the distance between the tip-sample distance from feedback to 10 microns above the sample using the z piezo electric of the tip to accurately retract the tip from the graphene-like platelet surface. Spectra collected with the tip located at 1, 5 and 10 microns above the sample are shown in supplementary information section (SI2) and shows that the far-field signal (tip located at 5 or 10 microns) is significantly weaker using our experimental conditions (200 μW at the sample). The z-distance dependence of the Raman signal graph (G mode at 1580 cm^{-1}, 20 s acquisition time per spectrum) is shown in Fig. 7b using a log scale for the tip-sample axis. A linear scale representation is provided in the supplementary information section (SI3). Interestingly, Fig.7b highlights two distinct regimes. A first decrease is observed within the first 20 nm. This reveals the near-field nature of the TERS signal that is enhanced only when the tip is within the first 20 nm above the sample. A second regime in the 20-1000 range and that varies linearly is presumably the enhancement from the back scattering of the tip located within the focal volume of the focussed excitation laser. As shown by the scattering maps in Fig. 2, there is an intense Rayleigh scattering from the tip which acts as a mirror thus enhancing also the Raman signal of the graphene. When the tip is completely out of focal volume (i.e. above 1-2 micron), the signal is constant (SI2) and is similar to a micro-Raman measurement in a transmission geometry.

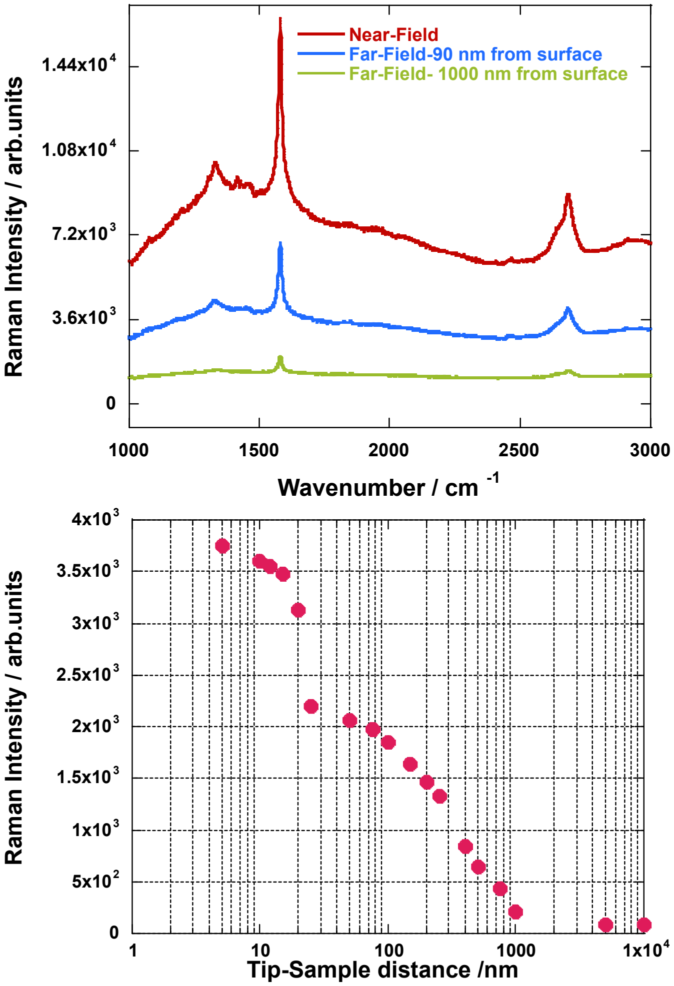

Figure 7: (a) Tip-enhanced Raman spectra measured in Near-field and Far-field (b) Raman intensity versus tip-sample distance in log scale of the G mode

An estimate of the enhancement factor of the TERS experiments can be done using the observations reported bove. Enhancement factors (EF) were calculated for the G band. First the contrast was determined using Equation (1),

$$C = \frac{I_{TERS}-I_0}{I_0} \qquad (1)$$

where I_0 and I_{TERS} represent the intensity of the Raman signal with the tip away and in proximity with the sample, respectively. The overall enhancement factor depends on the ratio of the illuminated areas in the far-field (~ $d_L{}^2$) and the near-field (~$d_{tip}{}^2$) conditions. The EF can then be estimated using Equation (2),

$$EF = C\,\frac{d_L^2}{d_{tip}^2} \qquad (2)$$

where $d_{L=}1$ μm and $d_{tip=}$ 0.02μm are the diameters of the laser spot and the tip, respectively. Contrast factors calculated using C(G) = 18 with I_{TERS}=3960 and I_0=206, provides a crude approximation of the enhancement factor in the range of ~4.5×10^4 for the G band. If we now consider the possible mirror effect from the tip, the contrast factor is significantly reduced to C(G)~0.8 with I_{TERS}=3960 and I_0=2200 (Raman intensity of the G mode measured at z=20 nm) yielding and enhancement factor of ~2×10^3. Although these are crude approximations they are comparable to the distribution of TERS enhancement values reported in the literature.[55]

Conclusions

In this study, we have shown that the sensitivity of TERS is well adapted to study the edges of graphene-like graphite material. The spatial resolution provided by TERS allows one to probe specifically the edges of graphene flakes. Due to the large scattering cross section of graphene and in general carbon-containing materials, TERS was successfully used to probe graphene-like graphite flakes deposited on gold nanoplates. The gap mode TERS associated with distinct polarizations of the excitation beam allowed one to discriminate the edges of an individual graphene flake composed of a few layers with a resolution of <20 nm. The analysis of the Raman spectra and intensity ratio of the D/G Raman modes provides valuable information to determine edge type and orientation of the graphene flakes. TERS appears as a critical surface technique providing surface molecular information signal as well as high spatial resolution in the 10-20 nm range. Future work on functionalized graphene or decorated graphene with metallic particles will be conducted using this approach.

Acknowledgements

The authors gratefully acknowledge the Nanofabrication Facility at The University of Western Ontario. GF and FLL both acknowledge the Natural Sciences and Engineering Research Council of Canada Discovery Grant program and the Canada Research Chairs program.

Notes and references

[a] Department of Chemistry, Department of Physics & Astronomy and Centre for Advanced Materials and Biomaterials Research, University of Western Ontario , 1151 Richmond Street, London, Ontario, N6A 5B7, Canada. E-mail: flagugne@uwo.ca

[b] Department of Chemistry, Department of Physics and Centre for Advanced Materials and Biomaterials Research, University of Western Ontario , 1151 Richmond Street, London, Ontario, N6A 5B7, Canada.

1. Y. Zhang, Y.-W. Tan, H. Stormer and P. Kim, *Nature*, 2005, **438**, 201-204.
2. A. Geim and K. Novoselov, *Nat. Mater.* , 2007, **6**, 183-191.
3. A. Ferrari, J. Meyer, V. Scardaci, C. Casiraghi, M. Lazzeri, F. Mauri, S. Piscanec, D. Jiang, K. Novoselov, S. Roth and A. Geim, *Phys. Rev. Lett.* , 2006, **97**, 187401.
4. A. C. Ferrari, *Solid State Commun.* , 2007, **143**, 47–57.
5. C. Casiraghi, A. Hartschuh, H. Qian, S. Piscanec, C. Georgi, A. Fasoli, K. S. Novoselov, D. M. Basko and A. C. Ferrari, *Nano Lett.*, 2009, **9**, 1433-1441.
6. F. Schedin, E. Lidorikis, A. Lombardo, V. G. Kravets, A. K. Geim, A. N. Grigorenko, K. S. Novoselov and A. C. Ferrari, *ACS Nano*, 2010, **4**, 5617-5626.
7. W. Xu, X. Ling, J. Xiao, M. S. Dresselhaus, J. Kong, H. Xu, Z. Liu and J. Zhang, *Proc. Natl. Acad. Sci.* , 2012, **109**, 9281-9286.
8. Y. Zhao, X. Liu, D. Y. Lei and Y. Chai, *Nanoscale*, 2014, **6**, 1311-1317.
9. A. N. Sidorov, G. W. Sławiński, A. H. Jayatissa, F. P. Zamborini and G. U. Sumanasekera, *Carbon*, 2012, **50**, 699-705.
10. L. Zhou, H. Gu, C. Wang, J. Zhang, M. Lv and R. He, *Colloid Surface A*, 2013, **430**, 103-109.
11. B.-S. Yeo, J. Stadler, T. Schmid, R. Zenobi and W. Zhang, *Chem. Phys. Lett.* , 2009, **472**, 1–13.
12. S. G. Zhang, X. W. Zhang, X. Liu, Z. G. Yin, H. L. Wang, H. L. Gao and Y. J. Zhao, *Appl. Phys. Lett.*, 2014, **104**, 121109.
13. R. M. Stöckle, Y.-D. Suh, V. Deckert and R. Zenobi, *Chem. Phys. Lett.*, 2000, **318**, 131–136.
14. N. Hayazawa, Y. Inouye, Z. Sekkat and S. Kawata, *Chem. Phys. Lett.*, 2001, **335**, 369–374.
15. P. Verma, T. Ichimura, T. Yano, Y. Saito and S. Kawata, *Laser. Photonics. Rev*, 2010, **4**, 548-561.
16. C. C. Neacsu, S. Berweger and M. B. Raschke, *J. Nanobiotechnology*, 2009, **3**, 172–196.
17. J. Stadler, T. Schmid and R. Zenobi, *Nano Lett.*, 2010, **10**, 4514-4520.
18. M. Nicklaus, C. Nauenheim, A. Krayev, V. Gavrilyuk, A. Belyaev and A. Ruediger, *Rev. Sci. Instrum.*, 2012, **83**, 066102.
19. A. Hartschuh, *Angew. Chem.* , 2008, **47**, 8178-8191.
20. S. Vantasin, I. Tanabe, Y. Tanaka, T. Itoh, T. Suzuki, Y. Kutsuma, K. Ashida, T. Kaneko and Y. Ozaki, *J. Phys. Chem. C*, 2014, **118**, 25809-25815.
21. A. Hartschuh, H. Qian, C. Georgi, M. Böhmler and L. Novotny, *Anal. Bioanal. Chem.*, 2009, **394**, 1787-1795.
22. T. Suzuki, T. Itoh, S. Vantasin, S. Minami, Y. Kutsuma, K. Ashida, T.-A. Kaneko, Y. Morisawa, T. Miura and Y. Ozaki, *Phys. Chem. Chem. Phys.*, 2014, **16**, 20236-20240.
23. N. Kazemi-Zanjani, H. Chen, H. Goldberg, G. Hunter, B. Grohe and F. Lagugné-Labarthet, *J. Am. Chem. Soc.*, 2012, **1234**, 17076-17082.
24. T. Schmid, L. Opilik, C. Blum and R. Zenobi, *Angew. Chem.*, 2013, **52**, 5940-5954.
25. B. Pettinger, P. Schambach, C. J. Villagomez and N. Scott, *Annu. Rev. Phys. Chem.*, 2012, **63**, 379-399.
26. G. Picardi, M. Chaigneau, R. Ossikovski, C. Licitra and G. Delapierre, *J. Raman Spectrosc.*, 2009, **40**, 1407-1412.
27. M. D. Sonntag, J. M. Klingsporn, L. K. Garibay, J. M. Roberts, J. A. Dieringer, T. Seideman, K. A. Scheidt, L. Jensen, G. C. Schatz and R. P. Van Duyne, *J. Phys. Chem. C*, 2012, **116**, 478-483.

28. J. M. Klingsporn, N. Jiang, E. A. Pozzi, M. D. Sonntag, D. Chulhai, D. Seideman, L. Jensen, M. C. Hersam and R. P. Van Duyne, *J. Am. Chem. Soc.*, 2014, **136**, 3881-3887.
29. Y. Fang, Z. Zhang, L. Chen and M. Sun, *Phys. Chem. Chem. Phys.*, 2015, **17**, 783-794.
30. T. Deckert-Gaudig, E. Bailo and V. Deckert, *J. Biophoton*, 2008, **1**, 377-389.
31. E. Bailo and V. Deckert, *Chem. Soc. Rev.*, 2008, **37**, 921-930.
32. Z. Yang, J. Aizpurua and H. Xu, *J. Raman Spectrosc.*, 2009, **2009**, 1343-1348.
33. N. Kazemi-Zanjani, S. Vedraine and F. Lagugné-Labarthet, *Opt. Express*, 2013, **21**, 25271-25276.
34. T. Deckert-Gaudig and V. Deckert, *Small*, **5**, 432-436.
35. T. Deckert-Gaudig, E. Bailo and V. Deckert, *Phys. Chem. Chem. Phys.*, 2009, **11**, 7360-7362.
36. F. Pashaee, R. Hou, P. Gobbo, M. S. Workentin and F. Lagugné-Labarthet, *J. Phys. Chem. C*, 2013, **117**, 15639-15646.
37. T. Deckert-Gaudig, E. Rauls and V. Deckert, *J. Phys. Chem. C*, 2010, **114**, 7412-7420.
38. B.-S. Yeo, E. Amstad, T. Schmid, J. Stadler and R. Zenobi, *Small* 2009, **5**, 952-960.
39. T. A. Yano, P. Verma, Y. Saito, T. Ichimura and S. Kawata, *Nat. Photonics.*, 2009, **3**, 473 - 477.
40. A. Shiotari, T. Kumagai and M. Wolf, *J. Phys. Chem. C*, 2014, **118**, 11806-11812.
41. K. F. Domke and B. Pettinger, *J. Raman Spectrosc.*, 2009, **40**, 1427-1433.
42. Y. Saito, P. Verma, K. Masui, Y. Inouye and S. Kawata, *J. Raman Spectrosc.*, 2009, **40**, 1434-1440.
43. J. Stadler, T. Schmid and R. Zenobi, *ACS Nano*, 2011, **5**, 8442-8448.
44. H.-C. Chu, C.-H. Kuo and M. H. Huang, *Inorg. Chem.*, 2006, **45**, 808-813.
45. Z. Wu, Z. Chen, X. Du, J. M. Logan, J. Sippel, M. Nikolou, K. Kamaras, J. R. Reynolds, D. B. Tanner, A. F. Hebard and A. G. Rinzler, *Science*, 2004, **305**, 1273-1276.
46. G. Eda, G. Fanchini and M. Chhowalla, *Nat. Nano*, 2008, **3**, 270-274.
47. F. Sharifi, R. Bauld, M. S. Ahmed and G. Fanchini, *Small*, 2012, **8**, 699-706.
48. A. Merlen, J. Plathier and A. Ruediger, *Phys. Chem. Chem. Phys.*, 2015, advanced article.
49. S. Viarbitskaya, A. Teulle, R. Marty, J. Sharma, C. Girard, A. Arbouet and E. Dujardin, *Nat. Mater.*, 2013, **12**, 426-432.
50. A. C. Ferrari and D. M. Basko, *Nat. Nano.*, 2013, **8**, 235-246.
51. B. Krauss, P. Nemes-Incze, V. Skakalova, L. P. Biro, K. von Klitzing and J. H. Smet, *Nano Lett.*, 2010, **10**, 4544-4548.
52. P. Wang, D. Zhang, L. Li, Z. Li, L. Zhang and Y. Fang, *Plasmonics*, 2012, **7**, 555-561.
53. Z. Luo, S. Kim, N. Kawamoto, A. M. Rappe and A. T. C. Johnson, *ACS Nano*, 2011, **5**, 9154-9160.
54. N. Kazemi-Zanjani, P. Gobbo, Z. Zhu, M. S. Workentin and F. Lagugné-Labarthet, *Can. J. Chem*, 2015, **93**, 51-59.
55. R. V. Maximiano, R. Beams, L. Novotny, A. Jorio and L. G. Cançado, *Phys. Rev. B*, 2012, **85**, 235434.